Liquefaction source layer for sand blows induced by the 2016 megathrust earthquake (Mw 7.8) in Ecuador (Boca de Briceño)

Aura C. Salocchi[a], Luca Minarelli[b], Stefano Lugli[a], Sara Amoroso[b, c], Kyle M. Rollins[d], Daniela Fontana[a*]

a Department of Chemical and Geological Sciences, University of Modena and Reggio Emilia, 41125 Modena, Italy

b Istituto Nazionale di Geofisica e Vulcanologia, 67100 L'Aquila, Italy.

c Department of Engineering and Geology, University of Chieti-Pescara, 65129 Pescara, Italy

d Department of Civil and Environmental Engineering, Brigham Young University, UT 84602, USA.

* corresponding author, daniela.fontana@unimore.it

Abstract

Numerous sand boils were generated in the alluvial plain at the mouth of the Rio Briceño valley (Ecuador) during the Mw 7.8 earthquake of April 2016. The area is characterized by a series of raised marine terraces formed as a consequence of the rapid tectonic coastal uplift during the Quaternary. On the basis of boreholes and geognostic investigations carried out within a mitigation project for liquefaction below a highway embankment and during post-earthquake surveys, we recognized 5 lithological units in the subsurface, reflecting the continental-marine and transitional sedimentation since the Last Glacial Maximum. We performed a comprehensive study of texture and petrographic composition of sand boils compared with sandy silts and silty sands of the buried sedimentary sequence in order to identify the source levels for liquefaction. The petrographic components, in particular the low content of bioclasts and carbonate fragments of the sand boils, allow to pinpoint a source layer made up of fine-grained silty sands located between 2 and 4.5 m depth (unit 2) whereas the deeper marine sands, richer in bioclasts, were not involved. The results support the idea that earthquake-induced liquefaction phenomena are not restricted to clean sands and well-sorted deposits, but may affect sand layers with significant amount of non-plastic silt.

Keywords: Earthquake-induced liquefaction, Sand blows, Ecuadorian coast, Sand composition, Holocene depositional sequences

1. Introduction

Several liquefaction phenomena occurred as a consequence of a strong earthquake (M_w7.8) of April 2016 along the central Pacific coastline of Ecuador (GEER-ACT, 2016; Chunga et al., 2017). The earthquake was located onshore, less than 10 km southeast of the city of Pedernales, with a hypocentral depth of 21 km, rupturing the central seismogenetic segment of the South American subduction zone. In this area, the study of the liquefaction phenomena is particularly significant because frequent and very strong earthquakes are generated by megathrusts in a geological context characterized by continuous uplift and high sedimentation rate providing a complex stratigraphic architecture. In particular, the sediments involved in the liquefaction phenomena belong to the high-frequency sedimentary cycles related to the Quaternary climatic oscillations, which are extremely well recorded in the marine-continental successions. Moreover, the study of liquefaction effects is particularly relevant considering that these coastal areas contain urban centres, infrastructure and communication networks, that were recently the object of innovative mitigation strategies (Smith and Wissmann 2018, Vera-Grunauer et al. 2019, Amoroso et al. 2020a).

The aim of this research is to define the stratigraphic architecture of the shallow subsurface of the Boca de Briceño area in order to identify the source levels for liquefaction, using the texture and composition of sand boils compared with the buried sedimentary sequence. The study also may provide insights into ejection mechanisms in regions impacted by frequent earthquakes that triggered recurrent liquefaction (Giona Bucci et al., 2018; Maurer et al., 2019) and contribute in evaluating the success of a mitigation project carried out below a highway embankment in this area.

2. Geological setting

The study area is located on the coast of mainland Ecuador, a zone of intense crustal deformation due to the subduction of the Nazca oceanic plate beneath the South-American continental plate (Fig. 1). The subduction occurs along a N90°E direction at a rate of 58-78 mm/a (Trenkamp et al., 2002). The subduction induces a shortening perpendicular to the trench axis and, in turn, the expulsion of the north Andean block to the Northeast along the Guayaquil Caracas Megashear, with a rate of ∼6 to 10 mm/a (Kellogg and Vega, 1995; Ego et al., 1996; Trenkamp et al., 2002). Recently, before the 2016 earthquake (M_w 7.8), the Ecuadorian shoreline experienced strong megathrust earthquakes: in 1906 (estimated Mw 8.8, 600-km long rupture area, one of the strongest earthquake registered on our planet), 1942 (M_w 7.8), 1958 (M_w 7.7), and 1979 (M_w 8.2).

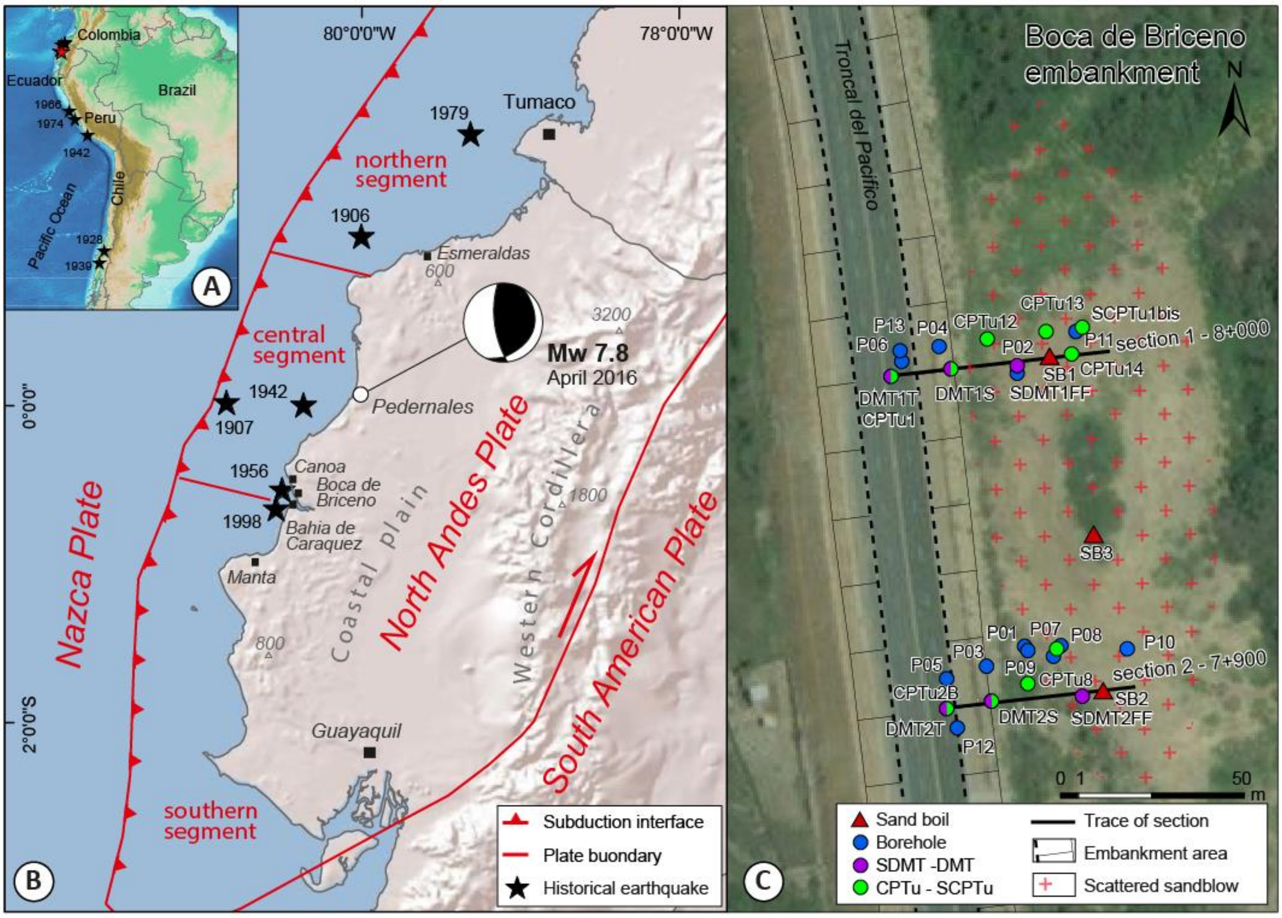

Fig. 1 Location (A) and seismotectonic map (B) of the Briceño Bridge area in Ecuador with indication of the historical earthquakes (modified after Amoroso et al., 2020 and Chunga et al. 2018). Study area with location of sand blows and boreholes (C).

The Colombia–Ecuador subduction trench is characterized by rapid sedimentation due to a tropical climate and orographic rains on the western Andean slope caused by the prevailing Pacific winds. The trench contains a thick sedimentary infill, up to 3 km-thick, probably due to recent turbidites associated with hemipelagic sedimentation. The high sediment thickness along the subducting margin seems to influence the large ruptures associated with great megathrust earthquakes. The subduction of large volumes of sediments creates a sort of homogenous plate interface, which allows the seismic ruptures to overcome the bathymetric barriers, propagating the trench-parallel ruptures (Alvarez et al., 2017).

The Ecuadorian margin substratum consists of the oceanic North-Andean block accreted to the Brazilian continental craton during the Cretaceous (Jaillard et al., 1997). The oceanic terranes are made up of tholeiitic-andesitic basalts and pillow lavas associated with siliceous sediments (Piñon Formation) overlain by intra-oceanic volcanic arc sequences (Cayo formation, Jaillard et al., 1995; Reynaud et al., 1999).

The coastal area of Ecuador (Talara Arc) is actively uplifted along a concave subduction zone. The uplift is related to the eastward subduction of the aseismic Carnegie Ridge, which is part of the oceanic Nazca plate. The active subduction of the ridge is responsible for great lateral variations in deformation, seismicity, magmatism and sediment deposition along the margin (Gutscher et al., 1999; Collot et al., 2002). The uplift rate in the coastal area of Ecuador ranges between 0.10 and 0.42 mm/a for the Late Quaternary (Pedoja et al., 2006). As a result of the rapid uplift, the coast is characterized by well-preserved, raised, marine terraces, called Tablazos, which show late Pliocene to Pleistocene high-frequency depositional sequences (Cantalamessa et al., 2001; Di Celma et al., 2002).

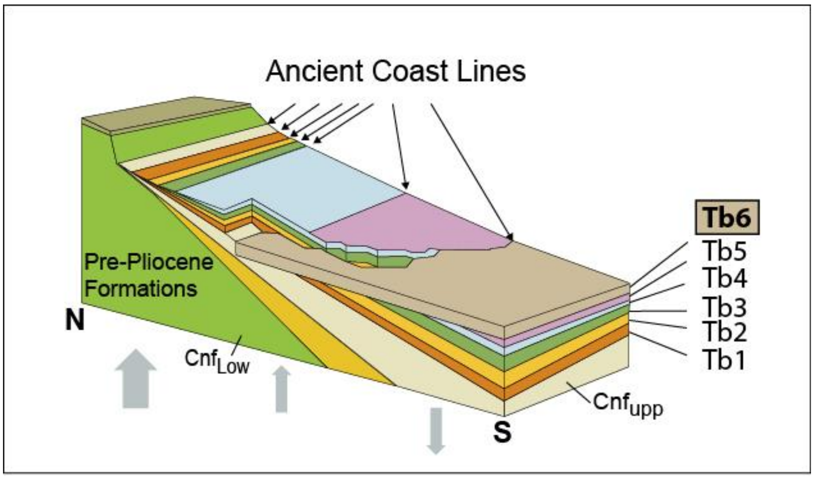

Fig. 2 Block diagram illustrating the Plio-Pleistocene stratigraphic architecture of costal Ecuador according to Cantalamessa and Di Celma (2004). CnF_{low}: lower Canoa Formation, CnF_{upp}: upper Canoa Formation. Tb: Cyclothems of the Tablazo Formation. The studied succession belongs to the Tb6 sequence.

2.1 The sedimentary sequence of the coastal margin

The combined effects of tectonic coastal uplift and Quaternary sea level fluctuations resulted in the formation of a series of raised marine terraces on the coastal stretch of mainland Ecuador. The Pliocene-Pleistocene coastal sequence was traditionally subdivided into the Canoa Formation and the Tablazo Formation (Sheppard, 1930). Di Celma et al. (2002) and Cantalamessa and Di Celma (2004) recognized up to four marine terraces in the area, while Pedoja et al. (2006) mapped up to five terraces. The significance of the terraces for the interpretation of the uplift rates of coastal Ecuador was stressed by Pedoja et al. (2006a, 2006b) and the cyclothemic nature of these formations was described in detail by Di Celma et al. (2002), Cantalamessa and Di Celma (2004).
According to Cantalamessa and Di Celma (2004), the sedimentary succession lies unconformably on pre-Pliocene deposits and reflects deposition in offshore, shoreface, and alluvial environments

(Fig. 2). The cyclothem consists of a deepening–shallowing upward facies association bounded by a ravinement surface, amalgamated with the preexisting sequence boundary. Each of the marine terraces formed during sea-level rise and highstand, and was progressively uplifted during a cycle of sea-level fluctuation. The terraces are composed of a wave-cut platform formed during the transgressive stage, covered by thin beach deposits consisting of sands, pebbles and shell fragments. The Canoa Formation lies unconformably over the Tosagua Formation (Early Miocene) and has been divided into two units with different deepening–shallowing facies associations, CnF_{low} (late Pliocene) and CnF_{upp} (Early Pleistocene), separated by an angular unconformity. The Tablazo Formation (Middle Pleistocene–Holocene) consists of at least six cyclothems characterized by a deepening–shallowing facies sequence. The cyclothems represent a single forced regressive sequence set.

Only in the last cyclothem (sequence Tb6, Fig. 2) the shallowing-upward part of the depositional sequence can be seen, differently from the lower cyclothems where the corresponding part of the sequence was eroded during the ravinement surface formation at each sequence boundary. Sequence Tb6 begins with a ravinement surface followed by a transgressive, deepening-upward shoreface succession, capped by a shallowing-upward shoreface to coastal-plain facies succession. In correspondence of the main fluvial entry points, the sequence is cut by valleys filled by estuarine sediments. The alluvial-estuarine deposits may contain Late Pleistocene–early Holocene continental vertebrate (Cantalamessa et al., 2001). The fluvial valleys, cut during sea level lowstands, were flooded and filled during the early phase of the Holocene transgression. As a whole, the depositional sequence seems to reflect the last cycle of sea-level fluctuation since MIS 5e, and represents the result of the sedimentation of the last 124 ka.

2.2 The Boca de Briceño area

The area is characterized by Mio-Pleistocene turbidite deposits and Quaternary alluvial and marine terraces consisting of gravels, sand, silt and clay, highly variable in thickness and lateral extent, cut by the Rio Briceño valley. Detailed post-earthquake surveys were performed to detect the numerous site effects developed in the area, as well as along the Ecuadorean coast (GEER-ACT 2016, Chunga et al. 2017). In particular, liquefaction phenomena were observed and studied at the Briceño embankment, approximately 7 km from Canoa city and 112 km from the earthquake epicenter (Fig. 1b). The estimated peak ground acceleration at the site was 0.4g (Ye et al., 2016, Beauval et al., 2017).

The earthquake shaking generated numerous sand boils in the alluvial plain (Fig. 1c), clustering in a wide elongated area next to the river mouth, a few hundreds of meters from the shoreline (Fig. 1c).

Sand boils were generally small, about 1 m across and a few centimetres high, and grew above a flat surface cut by mud cracks (Fig. 3).

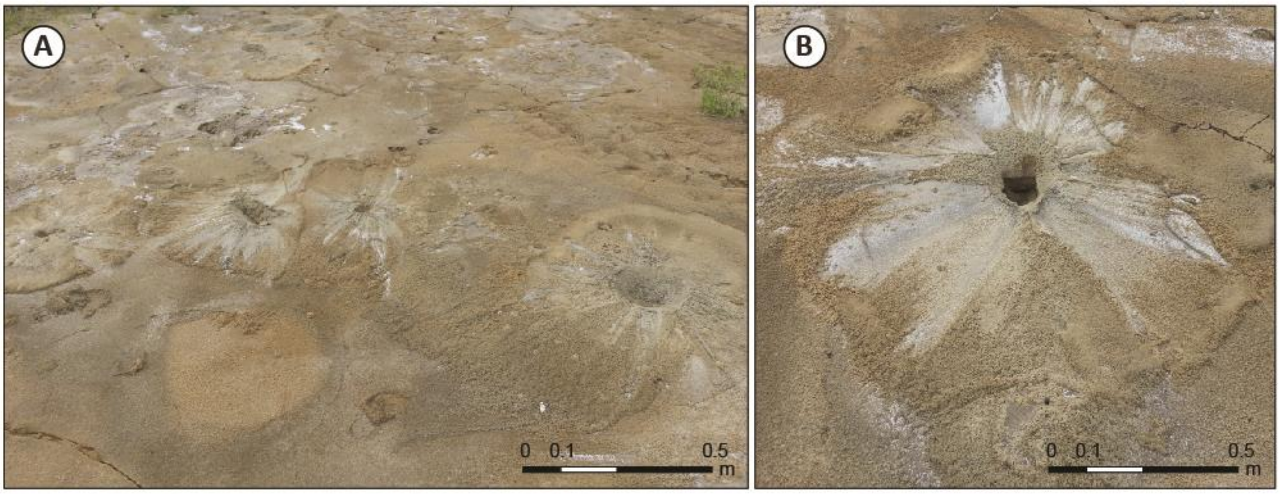

Fig. 3 Sand boils in the Briceño Bridge area photographed after the main shock, a few months later (A), and detail of a sand volcano (B).

As shown in Fig 1c, the sand boils are located in the area adjacent to the embankment, next to the bridge abutment, along the the Troncal de Pacifico Road. This infrastructure exhibited minimal damage due to the earthquake (GEER-ACT, 2016), likely as a result of a mitigation project to prevent liquefaction-induced failures (Smith and Wissmann 2018). Rammed aggregate pier® (RAP) ground improvement elements were used to reinforce foundation materials and to increase the stability of the sand deposits in the subsurface, which has been used successfully at similar sites in New Zealand (Wissmann et al., 2015 ; Wentz et al., 2015 ; Vauther in et al., 2017) and in Italy (Amoroso et al., 2020b).

In this context, an extensive geological and geotechnical site characterization campaign was performed mostly along two sections of the Briceño bridge embankment, with the aim of examining in depth the mechanisms involved in the liquefaction processes and evaluation of mitigation effectiveness (Smith and Wissmann, 2018; Amoroso et al., 2020a).

3. Methods and sampling

To reconstruct the stratigraphy of the area (Fig. 4), we based our observations on the complete dataset acquired during the mitigation project and subsequent post-earthquake investigations (Smith and Wissmann, 2018; Amoroso et al., 2020a). In particular we examined in detail cores from 13 boreholes: five log cores (P07, P08, P09, P10, P11) to a depth of 6 m, five log cores 12 m deep (P02 starting from the ground level and P03, P04, P05, P06 starting from the bridge embankment) and one core to a depth of 30 m (P01). The stratigraphic observations were supplemented by geotechnical data consisting of standard penetration test (SPT), Atterberg limits, 16 piezocone tests (CPTu), 4 seismic piezocone tests (SCPTu), 5 flat dilatometer tests (DMT) and 2 seismic dilatometer tests (SDMT). The location of cores and other investigations is reported in Fig. 1c.

Four boreholes (P07, P09, P10, P11) were sampled for textural (grain size) and compositional analyses (Fig. 4). The same textural and petrographic analyses were carried out on sand volcanoes from three different sites (samples SB1, SB2, SB3; with locations reported in Fig 1c).

Grain-Size Analyses. We analyzed eighteen samples from cores P07, P09, P10, P11 at different depths and from sand blows (Table 1, Fig. 5). Grain-size analyses were performed on the Mastersizer 3000 Laser granulometry (Low Angle Laser Light Scattering) at laboratories of the DSCG of the University of Modena and Reggio Emilia. Organic matter was removed from 80 g of samples by hydrogen peroxide (H_2O_2); the samples were air dried and mechanically sieved for granulometric and compositional analyses. About 0.5 g of sample were transferred into a 250 ml beaker filled by deionized water. The suspension was lit by the low-intensity laser beam; particle-size distribution data were obtained under constant agitation in the measuring beaker. A refractive index of 1.52 for the laser radiation (λ =750 nm), an absorption coefficient of 0.1 and a Dispersal Refractive Index of 1.33 for the total range were used. For each sample five measurements were taken for three aliquots, then averaged. Index properties were estimated using the grain size distribution, by means of the Atterberg limits, fines content (FC) which represents percentage of particles finer than 0.075 mm; the diameters of the 60th (D_{60}), 30th (D_{30}), and 10th (D_{10}) percentile of the granulometric curve; the coefficient of uniformity (U), given by the ratio between D_{60} and D_{10}; and the coefficient of curvature (C), function of D_{60}, D_{30}, and D_{10}.

Compositional Analyses. Point counting was performed on eleven samples under transmitted-light microscopy on the 0.125–0.250 mm fraction, according to the Gazzi-Dickinson method designed to minimize the dependence of the analysis on the grain size (Zuffa, 1985; Arribas and Tortosa, 2003). We distinguished 23 compositional categories reported in Table 2. Results are plotted in the traditional Q (quartz), F (feldspars), L (siliciclastic lithics) + C (carbonate) diagram (Fig. 6a) and are shown also in the Q+F, L, C plot (Fig 6b) that makes it possible to better differentiate the compositional fields in Quaternary sands, as discussed by Lugli et al. (2007).

4. **Results**

4.1 The Boca de Briceño sedimentary sequence

The studied sedimentary sequence can be divided into 5 main lithological units showing variable thickness. These units, detected in both sections of the bridge embankment shown in Fig. 4, are from the top to the bottom:

Unit 1, consisting of recent laminated silt and clayey silt with subordinate sandy layers, from the ground level to a depth ranging from 1.35 to 3.50 m; the unit locally fills paleochannels and may reach the depth of 5 m (section 1).

Unit 2, consisting of silty sands with rare seashell beds, with variable thickness within the studied area; the top of the unit ranges from 1.35 to 3.5 m depth, and its base from 3.8 to 5.50 m depth.

Unit 3 is very thin (maximum 1 m thick) and discontinuous, made up of clayey silt with subordinate sands, and it has been recognized only in the southern area (section 2 in Fig. 4) at the depth of 4 m.

Unit 4 consists mainly of coarse-grained sands and minor pebbles with abundant seashell beds. The top of the unit ranges from 3.8 to 5.50 m depth and the bottom from 9.00 m (P01) to more than 12 m depth (P02 hole bottom).

Unit 5, consists of compacted silty and clayey sediments with subordinate silty sands and widespread oxidation traces. The top of the unit is detected at a depth varying from 9.00 m to more than 12 m, and it extends down to a depth of 28.65 m (P01 hole bottom).

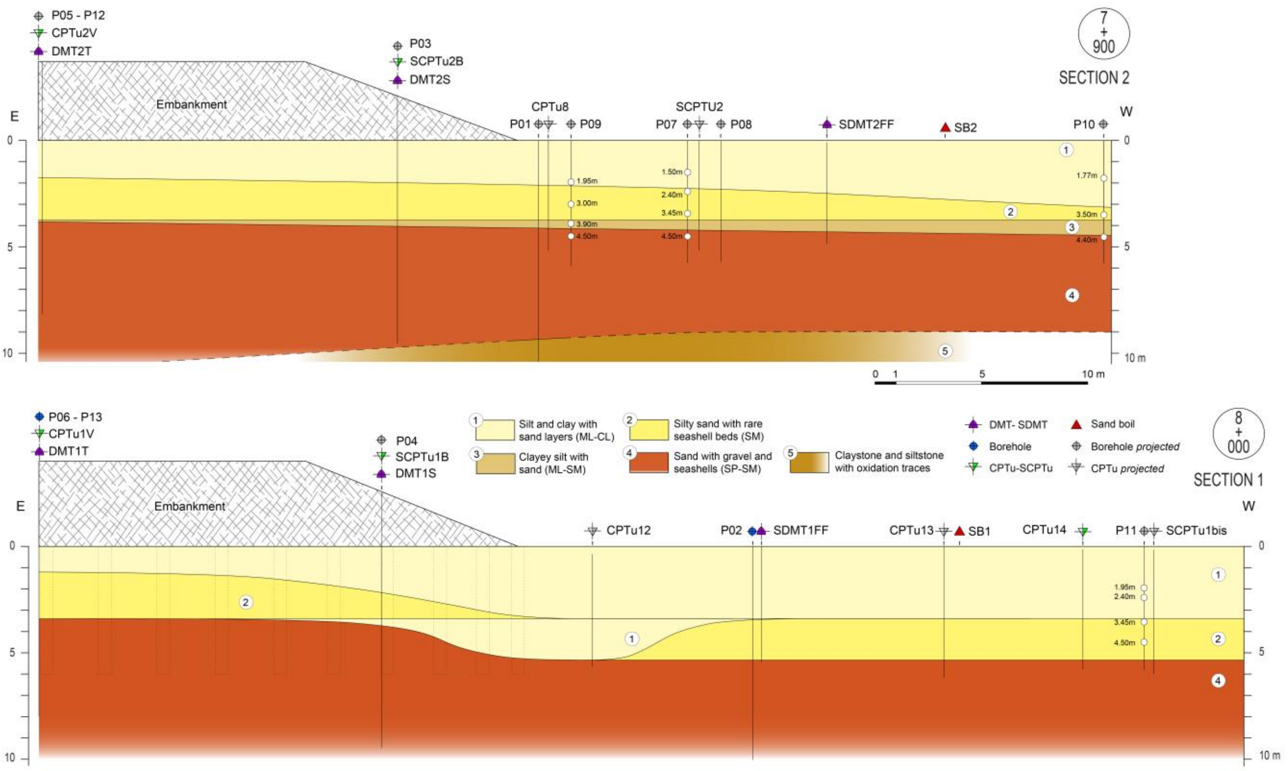

Fig. 4 Stratigraphic scheme of the successions involved in the liquefaction in the Briceño Bridge area showing the boreholes, the geotechnical tests (modified from Amoroso et al., 2020b) and the reconstructed lithological units across two sections (section 1 and section 2; see Fig. 1 for location).

4.3 Grain-size

The grain-size of the examined core samples ranges from almost pure sand to sandy silt (Fig. 5); the silt fraction varies from 10 to 60%, but the amount of clay is always less than 10%. An increase in grain size is observed with depth: finer samples characterize the shallow portion of the cores (at 1.5 to about 2 m depth below the ground level). From 2 to 4.5 m sands are fine to medium-grained (in two samples a coarse-grained fraction is also present) and the silty fraction is less than 40% (with the exception of sample P11_450, which is characterized by a higher amount of silt, about 50%). The sand volcanoes are made up of fine sands, and the three examined samples perfectly overlap despite belonging to different liquefaction sites. The amount of silt is around 30% and clay is less than 5%.

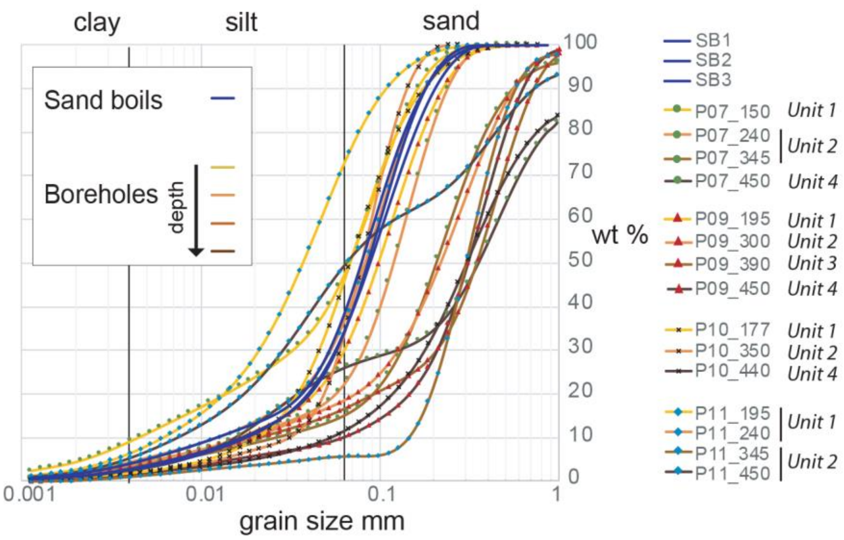

Fig. 5 Cumulative grain-size distributions of examined samples from cores at different depths and from sand blows (in blue).

The grain size analyses and the calculated index properties were then used to provide the USCS classification (ASTM D2487-11, 2011), reported in Table 1. Samples from shallow unit 1 are sandy silt (ML), whereas samples from deeper units 2 and 3 are silty sand (SM). The index properties (Table 1) indicate a similar high fines content in both the silty sand (SM) layers (FC ≈ 17-53%), and in the sand blows (FC ≈ 43-48%). The samples from the boreholes and the sand blows are well-graded (i.e., they contain particles with a wide range of sizes), as shown by the coefficients of curvature C and uniformity U. Atterberg limits confirmed that all the samples are non-plastic.

Samples	Description/Depth	FC (%)	D60 (mm)	D30 (mm)	D10 (mm)	U	C	USCS classification
P07_150	Section 2 - Borehole P07 1.50 m	55.64	0.0832	0.0324	0.0045	18.6	2.8	Sandy silt (ML)
P07_240	Section 2 - Borehole P07 2.40 m	27.41	0.1401	0.0814	0.0177	7.9	2.7	Silty sand (SM)
P07_345	Section 2 - Borehole P07 3.45 m	17.07	0.2502	0.1322	0.0263	9.5	2.7	Silty sand (SM)
P07_450	Section 2 - Borehole P07 4.50 m	27.24	0.4594	0.1245	0.0155	29.6	2.2	Silty sand (SM)
P09_195	Section 2 - Borehole P09 1.95 m	37.22	0.1182	0.0634	0.0163	7.3	2.1	Silty sand (SM)
P09_300	Section 2 - Borehole P09 3.00 m	20.52	0.2692	0.1256	0.0195	13.8	3.0	Silty sand (SM)
P09_390	Section 2 - Borehole P09 3.90 m	18.24	0.4101	0.2060	0.0210	19.5	4.9	Silty sand (SM)
P09_450	Section 2 - Borehole P09 4.50 m	11.62	0.3621	0.2072	0.0616	5.9	1.9	Poorly graded sand with silt (SP-SM)
P10_177	Section 2 - Borehole P10 1.77 m	56.00	0.0820	0.0457	0.0207	4.0	1.2	Sandy silt (ML)
P10_350	Section 2 - Borehole P10 3.50 m	46.69	0.0902	0.0597	0.0312	2.9	1.3	Silty sand (SM)
P10_440	Section 2 - Borehole P10 4.40 m	13.60	0.3867	0.1767	0.0527	7.3	1.5	Silty sand (SM)
P11_195	Section 1 - Borehole P11 1.95 m	80.03	0.0466	0.0210	0.0062	7.6	1.5	Silt with sand (ML)
P11_240	Section 1 - Borehole P11 2.40 m	45.51	0.0983	0.0530	0.0124	8.0	2.3	Silty sand (SM)
P11_345	Section 1 - Borehole P11 3.45 m	5.73	0.3458	0.2300	0.1450	2.4	1.1	Poorly graded sand with silt (SP-SM)
P11_450	Section 1 - Borehole P11 4.50 m	53.34	0.1213	0.0286	0.0074	16.5	0.9	Sandy silt (ML)
SB1	2016 sand boil	48.18	0.0936	0.0520	0.0122	7.7	2.4	Silty sand (SM)
SB2	2016 sand boil	43.42	0.1008	0.0571	0.0168	6.0	1.9	Silty sand (SM)
SB3	2016 sand boil	42.80	0.1059	0.0562	0.0178	5.9	1.7	Silty sand (SM)

Table 1. Index properties of the analyzed samples: FC is the fines content; D_{60}, D_{30}, and D_{10} are the diameters of the 60th, 30th, and 10th percentiles of the grain size distribution; U is the coefficient of uniformity; C is the coefficient of curvature.

4.4 Composition of sands

The results from the modal analyses are reported in Table 2 and in the ternary diagrams of Fig. 6. The petrography under the optical microscope is shown in Fig. 7.

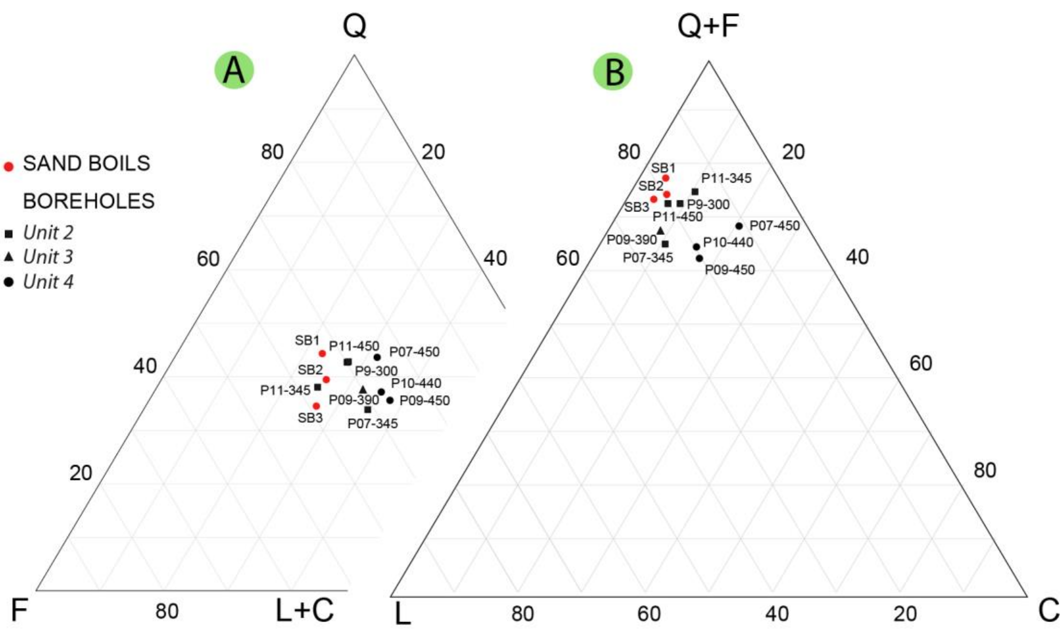

Fig. 6 Ternary diagrams Q,F, L+C and Q+F, L, C showing the composition of examined sands from cores (numbers refer to depth) and from liquefied sand boils (in red). Q, total quartz; F, total feldspars; L, siliciclastic lithic fragments; C, carbonate fragments.

In general, sands from the cores are made up of quartz (single crystal and polycrystalline) ranging from 28.0 to 37.3% of the bulk rock. Total feldspars range from 20 to 33% and consist largely of plagioclase and subordinately K-feldspar (orthoclase and microcline). Both quartz and feldspar grains are angular. Siliciclastic lithic fragments are made up primarily of volcanites (with microcrystalline groundmass with feldspar phenocrysts), spilites and serpentinites. Low-grade metamorphic rocks are minor components consisting of mica schist and phyllades. Sedimentary rocks include siltstones and shale. Siliciclastic lithics account for 9 to 21% of the whole rock.

Carbonate grains (6 to 16.3%) are made of bioclasts (benthic foraminifera, algae) (Fig. 7b), calcite spar and micritic grains. The amount of bioclasts is higher in the deeper samples (at depth of 4.5 m) and significantly decreases in the shallower samples (from 3.9 to 3.0 m depth).

Other significant components are micas, biotite, muscovite and chlorite, amphibole (mainly hornblende, green and brown), pyroxene and garnet. Glauconite is present in small amounts (less than 1%) in several samples. Opaque minerals (pyrite) and Fe-oxides are subordinate components.

In all the studied sands, grains are angular to subangular.

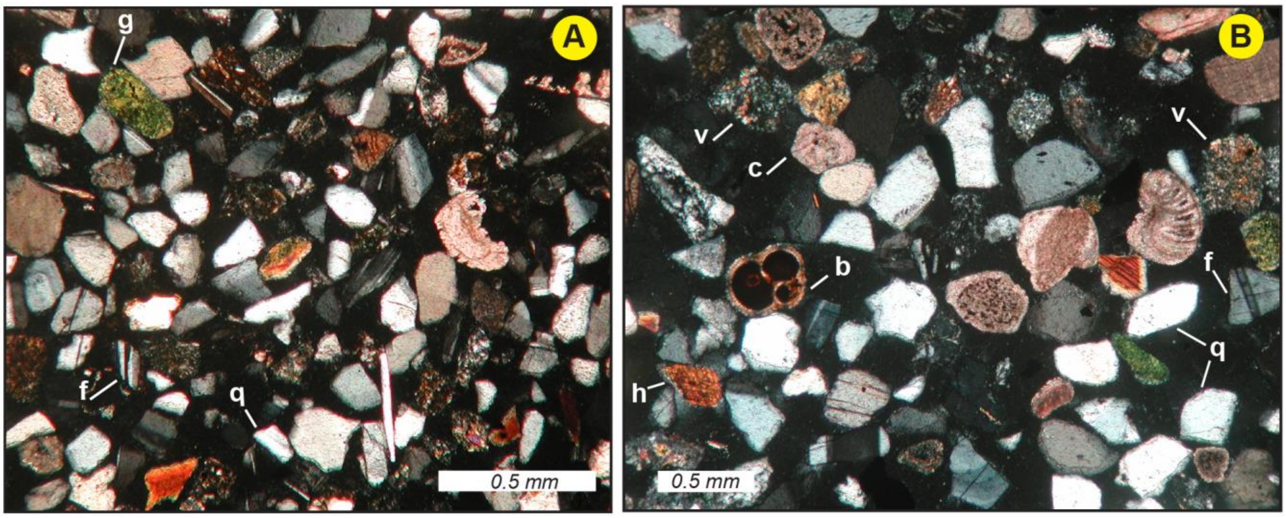

Fig. 7 Photomicrographs of the examined sands. A) sand blow (sample SB1) and B) core sample (P09_450), showing the main components, q: quartz, f: feldspars, b: bioclasts, c. calcite spar, v. volcanics, h. hornblende, g. glauconite. Transmitted light, crossed polars.

The composition of the sands indicate provenance from the erosion of the metamorphic/magmatic basement and volcanic rocks. Subordinate contributions are from sedimentary units (largely Miocene turbidite successions), in turn recycling basement lithotypes.

Samples from sand blows have a quite homogeneous composition with the same components described for the core sands. Mainly based on the low amounts of carbonates, which consist largely of bioclasts, the ejected sands show similarities with the shallower sands of unit 2. The similarity among samples is assessed by the Ward distribution, calculated using all the petrographic parameters (Fig. 8).

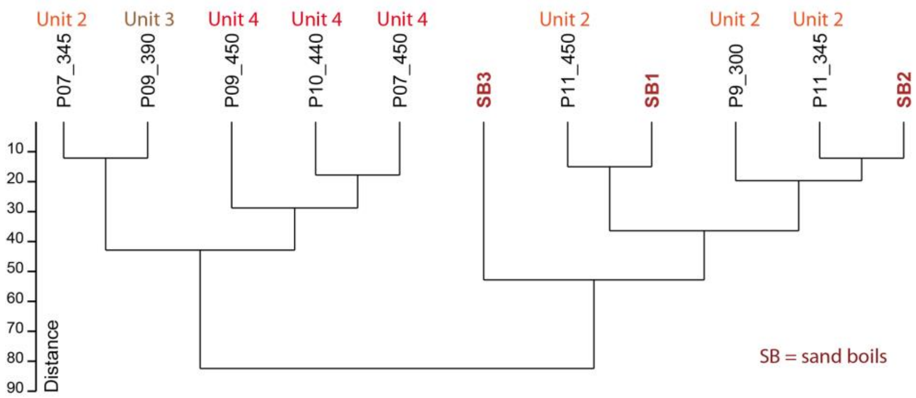

Fig. 8 Dendrogram showing the distribution of samples calculated using all the petrographic parameters. Ward's method. Similarity index: Euclidean.

		Boreholes								Sand boils		
		P07_345	P07_450	P09-300	P09_390	P09_450	P10_440	P11_345	P11_450	SB1	SB2	SB3
Q	Quartz single crystal	27,3	33,3	33,3	27,0	25,3	29,3	31,3	35,0	35,0	31,7	28,7
	Quartz polycrystalline	1,0	1,7	1,3	2,3	1,0	2,0	1,0	1,3	2,7	1,7	3,0
	Quartz in Rock fragment (r.f.)	0,3	0,3	1,0	1,0	1,7	0,0	1,7	1,0	1,3	0,3	0,7
F	K-feldspar single crystal	4,7	3,7	8,7	4,0	6,7	6,0	11,0	3,3	7,0	10,0	4,3
	K-feldspar in r.f.	0,3	0,0	0,0	0,3	0,0	0,0	0,0	0,0	0,0	0,3	0,0
	Plagioclase single crystal	20,3	16,3	16,3	19,3	14,3	17,0	20,7	22,7	21,7	19,0	31,3
	Plagioclase in r. f.	1,0	0,0	0,0	0,7	0,0	0,0	1,3	0,0	0,3	0,3	0,7
L	Metamorphite	1,7	1,0	1,0	0,0	0,7	1,0	0,7	1,3	2,7	2,0	1,0
	Volcanite	8,0	5,0	7,0	8,7	10,0	6,0	5,0	7,0	9,3	6,3	12,0
	Spilite	2,0	0,7	1,3	1,3	0,3	0,7	2,3	2,3	1,0	1,3	2,7
	Serpentinite	1,7	0,0	0,7	0,3	1,0	0,0	0,0	0,7	1,7	1,0	1,0
	Siltite	3,7	1,7	0,7	2,3	1,0	3,7	1,7	3,0	0,3	3,3	1,7
	Shale	4,0	1,0	5,0	7,0	3,3	5,7	4,0	3,7	1,3	3,0	2,7
C	Calcite spar	0,3	1,7	1,7	0,7	1,7	1,3	3,3	0,7	0,3	1,7	0,3
	Micrite	1,3	1,0	3,3	1,3	2,3	1,0	2,0	1,0	1,0	0,3	0,7
	Bioclast	7,0	13,7	2,3	4,7	9,7	10,7	3,7	4,3	2,3	3,0	3,0
	Mica and Chlorite	2,7	7,3	7,0	2,3	7,3	4,7	3,7	2,3	3,3	7,0	3,3
	Heavy mineral (unspecified)	2,3	2,3	1,0	2,7	3,0	2,0	1,0	1,3	1,7	1,7	0,3
	Heavy mineral (anfibol)	4,3	3,0	3,0	4,3	5,0	1,3	2,3	3,0	4,3	1,7	1,0
	Glauconite	1,0	0,0	0,3	0,3	0,0	1,0	0,3	0,3	0,3	0,3	0,7
	Fe-oxide	2,0	0,7	2,7	2,3	0,0	1,3	0,0	2,3	0,7	1,3	0,0
	Opaque	2,3	4,7	1,7	5,0	4,7	3,7	1,3	2,0	1,3	1,3	0,0
	Undetermined	0,7	1,0	0,7	2,0	1,0	1,7	1,7	1,3	0,3	1,3	1,0
		100%	100%	100%	100%	100%	100%	100%	100%	100%	100%	100%

Table 2 Compositional modal analyses of examined sands (r.f., rock fragment). Composition is determined based on transmitted-light spectroscopy of the 125–250 mm fraction.

5. Discussion

5.1 Interpretation of the cored sequence

The data from the 13 cores and from the geotechnical tests support the reconstruction of a detailed stratigraphic scheme of Quaternary alluvial-marine sediments in the area and, in particular, of the upper succession (from 0 to 5 m deep) in which the liquefiable layers are located (Fig. 4). Using the described lithological characteristics and the sedimentary features recognizable from core pictures, we may infer the following depositional environments:

- continental, fluvial-estuarine, for unit 1 and unit 5,
- marine to transitional fluvial, relatively-low energy, for units 2 and 3,
- marine, relatively-high energy, for unit 4.

Using as a reference the facies analyses of Di Celma et al. (2002), the studied sequence can be attributed to the shallowing-upward segment of the last cyclothem, the sequence Tb6 of the depositional model of Cantalamessa and Di Celma (2004).

The relatively large thickness of the continental deposits in the lower part of the sequence, unit 5, which is at least 20 m-thick, suggests that this segment may represent the continental infill of the fluvial paleo-valley of the Briceño River. The paleo-valley would have been cut during the sea level lowstand corresponding to the Last Glacial Maximum. The valley was then flooded and filled during the early phase of the Holocene transgression. The transition between units 4 and 5 may represent the ravinement surface followed by a transgressive shoreface succession (unit 4). The coarser marine sands of unit 4 may represent the exposed upper shoreface, and the following finer marine sands of unit 2 would correspond to the shoreface environment migrating inland. Unit 3 may represent the transitional marine-fluvial-estuarine facies. The topmost continental influx of unit 1 would indicate the last evolution of the sequence during the high stand, producing the final regressive system tract made up of fluvial-estuarine mainly argillaceous sediments of the present-day Briceño River**.**

5.2 The source layer identification

The petrographic composition of the sands allows us to discriminate the studied lithological units. Sands of unit 4 are significantly richer in bioclasts and carbonate fragments relative to those of unit 2. The petrography of the liquefied sands that ejected to the surface as sand boils, compared with that of buried sands, provides an important constraint in the recognition of the source layer. Based on the compositional affinity, in particular the low amount of bioclasts and carbonate grains, as shown by the Q+F, L, C ternary diagram (Fig. 6B), the sand boils were probably ejected from the shallow silty sand level of unit 2, whereas the deeper coarser sands of unit 4 were not affected. The affinity between the ejected sands and those of unit 2 is also confirmed considering the whole petrographic composition illustrated in the Ward diagram (Fig. 8).

The grain-size results also support the petrographic data in attributing the ejected sands to unit 2. Although the grain-size alone can not provide precise indications of the source layer, in this case the deeper sands of unit 4, which are coarser than those of the sand boils, can not be the source layer even considering segregation processes during ejection. The attribution of the source layer for liquefaction to unit 2 is in agreement with the geotechnical assessment performed by Smith and Wissmann (2018) and Vera-Grunauer et al. (2019).

In general, this study seems to corroborate previous findings that earthquake-induced liquefaction phenomena are not restricted to clean sands and well-sorted deposits, but may affect sand layers with significant amount of non-plastic silt, as recently recognized in liquefied sands in the Po plain (Italy; Fontana et al., 2015, 2019; Amoroso et al. 2020b).

The dependence of liquefaction susceptibility with particle shape and roundness has been discussed in the literature (Garga and McKay, 1984; Vaid et al, 1985; Hird and Hassona, 1990; Ishihara 1993; Ashour and Norris, 1999; Ashmawy et al., 2003). In our case we observe a distinct angular shape of the grains suggesting that, as discussed by Ashmawy et al. (2003) this parameter is not necessarily an influencing factor for liquefaction, which depends primarily on the sediment texture, fabric and porosity.

6. Conclusions

- The study of the sands ejected at Rio Briceño valley (Ecuador) during the Mw 7.8 earthquake of April 2016 and the comparison with buried alluvial-marine Quaternary sediments, provided us with clues about the source layers identification.
- The composition and fabric characteristics, such as grain-size distribution, indicate that liquefaction processes affected mainly sand layers at depth of 2-4.5 m, and a relatively shallow source for the blowouts. The deeper coarser marine sands, characterized by higher amounts of carbonate grains, mainly bioclasts, were not affected by liquefaction.
- This study seems to corroborate previous findings that earthquake-induced liquefaction phenomena are not restricted to clean sands and well-sorted deposits, but may affect sand layers with significant amount of non-plastic silt.

Acknowledgement

A special thanks to “Geopier Foundation Company” (Davidson, North Carolina, USA) for financing the extensive geotechnical and geophysical investigations at Briceño bridge embankment, to "Geoestudios" (Guayaquil, Ecuador) for gently assisting the proper performance of the site campaign, and to Prof. Kervin Chunga (Universidad Estatal Península de Santa Elena, Ecuador) for kindly sharing cartographies and scientific information of the studied area. Sedimentological analysis are carried out whitin the project FAR2018 Unimore, Fontana.

REFERENCES

Alvarez, J. O., Schechter, D. S. (2017). Improving oil recovery in the Wolfcamp unconventional liquid reservoir using surfactants in completion fluids. Journal of Petroleum Science and Engineering, 157, 806-815.

Amoroso, S., Rollins, K.M., Wissmann, K., Minarelli, L. (2019). Estimation of lateral spreading by SPT, CPTU and DMT following the 2016 Mw7.8 Ecuador earthquake. Conference paper at 6th International Conference on Geotechnical and Geophysical Site Characterization. 7-11 September, 2020.

Amoroso, S., Rollins, K.M., Wissmann, K., Minarelli, L. (2020a). Estimation of lateral spreading by SPT, CPTU and DMT following the 2016 Mw7.8 Ecuador earthquake. Proceedings of the 6th International Conference on Geotechnical and Geophysical Site Characterization - ISC'6 Conference, 7-11 September 2020, Budapest, Hungary.

Amoroso, S., Rollins, K.M., Andersen, P., Gottardi, G., Tonni, L., García Martínez, M.F., Wissmann, K., Minarelli, L., Comina, C., Fontana, D., De Martini, P.M., Monaco, P., Pesci, A., Sapia, V., Vassallo, M., Anzidei, M., Carpena, A., Cinti, F., Civico, R., Coco, I., Conforti, D., Doumaz, F., Giannattasio, F., Di Giulio, G., Foti, S., Loddo, F., Lugli, S., Manuel, M.R., Marchetti, D., Mariotti, M., Materni, V., Metcalfe, B., Milana, G., Pantosti, D., Pesce, A., Salocchi, A.C., Smedile, A., Stefani, M., Tarabusi, G., Teza, G. (2020b). Blast-induced liquefaction in silty sands for full-scale testing of ground improvement methods: insights from a multidisciplinary study. Engineering Geology, 265, 17 pp, https://doi.org/10.1016/j.enggeo.2019.105437

Arribas, J., and Tortosa, A. (2003), Detrital modes in sedimenticlastic sands from first- order streams of the Iberian Range, Spain: the potential for sand generation of different sedimentary rocks: Sedimentary Geology, 159, p. 275–303.

Ashmawy, A., Sukumaran, B., Hoang, V. (2003). Evaluating the Influence of Particle Shape on Liquefaction Behavior Using Discrete Element Modeling. Proc. Offshore and Polar Engineering Conference.

ASTM D2487-11 (2011). Standard Practice for Classification of Soils for Engineering Purposes (Unified Soil Classification System).

Beauval, C., Marinière, J., Laurendeau, A., Singaucho, J.C., Viracucha, C., Vallée, M., Maufroy, E., Mercerat, D., Yepes, H., Ruiz, M., Alvarado, A. (2017). Comparison of observed ground motion attenuation for the 16 April 2016 Mw 7.8 Ecuador megathrust earthquake and its two largest aftershocks with existing ground motion prediction equations, Seismol. Res. Lett. 88(2A), pp. 287–299.

Cantalamessa, G., Di Celma, C., Bianucci, G., Carnevale, G., Coltorti, M., Delfino, M., G. Ficarelli, M. Moreno Espinosa, D. Naldini, P. Pieruccini, L. Ragaini, L. Rook, M. Rossi, G. Tito, D. Torre, G. Valleri, W. Lanini (2001). A new vertebrate fossiliferous site from the Late Quaternary at San José on the north coast of Ecuador: preliminary note. Journal of South American Earth Sciences, 14(3), 331-334.

Cantalamessa, G., Di Celma, C. (2004). Origin and chronology of Pleistocene marine terraces of Isla de la Plata and of flat, gently dipping surfaces of the southern coast of Cabo San Lorenzo (Manabı, Ecuador). Journal of South American Earth Sciences, 16(8), 633-648.

Chunga, K., Livio, F., Mulas, M., Ochoa-Cornejo, F., Besenzon, D., Ferrario, M.F., Michetti, A.M. (2018). Earthquake ground effects and intensity of the 16 April 2016 Mw 7.8 Pedernales, Ecuador, earthquake: implications for the source characterization of large subduction earthquakes. Bulletin of the Seismological Society of America, 108(6), pp. 3384-3397.

Di Celma, C., Ragaini, L., Cantalamessa, G., Curzio, P. (2002). Shell concentrations as tools in characterizing sedimentary dynamics at sequence-bounding unconformities: examples from the lower unit of the Canoa Formation (Late Pliocene, Ecuador). Geobios, 35, 72-85.

Ego, F., Sébrier, M., Lavenu, A., Yepes, H., Egues, A. (1996). Quaternary state of stress in the Northern Andes and the restraining bend model for the Ecuadorian Andes. Tectonophysics, 259(1-3), 101-116.

Fontana, D., Lugli, S., Dori, S. M., Caputo, R., Stefani, M. (2015). Sedimentology and composition of sands injected during the seismic crisis of May 2012 (Emilia, Italy): clues for source layer identification and liquefaction regime. Sedimentary Geology, 325, 158-167.

Fontana, D., Amoroso, S., Minarelli, L., Stefani, M. (2019). Sand Liquefaction Induced By a Blast Test: New Insights On Source Layer and Grain-Size Segregation Mechanisms (Late Quaternary, Emilia, Italy). Journal of Sedimentary Research, 89(1), 13-27.

Geotechnical Extreme Events Reconnaissance Association–Applied Technology Council (GEER-ATC). 2016 "Earthquake Reconnaissance, Mw 7.8, April 16th, 2016, Muisne, Ecuador", Nikolaou, S., X. Vera-Grunauer, and R. Gilsanz (Editors), Version 1b, 604 pp., 2016. doi: 10.18118/G6F30N.

Giona Bucci, M., Villamor, P., Almond, P., Tuttle, M., Stringer, M., Ries, W., Smith, C., Hodge, M., Watson, M. (2018). Associations between sediment architecture and liquefaction susceptibility in fluvial settings: the 2010–2011 Canterbury Earthquake Sequence, New Zealand. Eng. Geol. 237, 181–197.

Gutscher, M. A., Malavieille, J., Lallemand, S., Collot, J. Y. (1999). Tectonic segmentation of the North Andean margin: impact of the Carnegie Ridge collision. Earth and Planetary Science Letters, 168(3-4), 255-270.

Hammer, Ø., Harper, D.A.T., Ryan, P.D. (2001). PAST: Paleontological statistics software package for education and data analysis. Palaeontologia Electronica 4(1): 9pp. http://palaeo-electronica.org/2001_1/past/issue1_01.htm

Jaillard, E., Ordoñez, M., Benitez, S., Berrones, G., Jiménez, N., Montenegro, G., Zambrano, I. (1995). Basin development in an accretionary, oceanic-floored fore-arc setting: southern coastal Ecuador during late Cretaceous-late Eocene time.

Jaillard, E., Benitez, S., Mascle, G. H. (1997). Les déformationspaléogenes de la zone d'avant-arc sud-équatorienneen relation avec l'évolutiongéodynamique. Bulletin de la Société géologique de France, 168(4), 403-412.

Kellogg, J. N., Vega, V., Stallings, T. C., Aiken, C. L. (1995). Tectonic development of Panama, Costa Rica, and the Colombian Andes: constraints from global positioning system geodetic studies and gravity. Special papers Geological Society of America, 75-75.

Lugli, S., Marchetti Dori, S., Fontana, D., (2007). Alluvial sand composition as a tool to unravelthe Late Quaternary sedimentation of theModena Plain, northern Italy. In: Arribas,J., Critelli, S., Johnsson, M.J. (Eds.), Sedimentary Provenance and Petrogenesis: Perspectivesfrom Petrography and Geochemistry. Geological Society of America SpecialPaper 420, pp. 57–72.

Maurer B.W., Green R.A., Wotherspoon L.M., Bastin S. (2019) The Stratigraphy of Compound Sand Blows at Sites of Recurrent Liquefaction: Implications for Paleoseismicity Studies. Earthquake Spectra: August 2019, 35(3), 1421-1440. https://doi.org/10.1193/041818EQS097M

Pedoja, K., Ortlieb, L., Dumont, J. F., Lamothe, M., Ghaleb, B., Auclair, M., Labrousse, B. (2006). Quaternary coastal uplift along the Talara Arc (Ecuador, Northern Peru) from new marine terrace data. Marine Geology, 228(1-4), 73-91.

Pedoja, K., Dumont, J. F., Lamothe, M., Ortlieb, L., Collot, J. Y., Ghaleb, B., Ghaleb, M. Auclair, V. Alvarez, Labrousse, B. (2006). Plio-Quaternary uplift of the Manta Peninsula and La Plata Island and the subduction of the Carnegie Ridge, central coast of Ecuador. Journal of South American Earth Sciences, 22(1-2), 1-21.

Reynaud, C., Jaillard, É., Lapierre, H., Mamberti, M., Mascle, G. H. (1999). Oceanic plateau and island arcs of southwestern Ecuador: their place in the geodynamic evolution of northwestern South America. Tectonophysics, 307(3-4), 235-254.

Sheppard, G., (1930). The geology of South Western Ecuador. American Association of Petroleum Geologists Bulletin 14, 263–309.

Smith, M.E., Wissmann, K. (2018). Ground improvement reinforcement mechanisms determined for the Mw 7.8 Muisne, Ecuador, earthquake. In: 5th Geotechnical Earthquake Engineering and Soil Dynamics Conference: Liquefaction Triggering, Consequences, and Mitigation - GEESDV 2018, Austin, Texas, June 10-13, 2018, GSP 290, pp. 286-294.

Trenkamp, R., Kellogg, J. N., Freymueller, J. T., Mora, H. P. (2002). Wide plate margin deformation, southern Central America and northwestern South America, CASA GPS observations. Journal of South American Earth Sciences, 15(2), 157-171.

Vera-Grunauer, X.F., Lopez-Zhindon, S., Ordonez-Rendon, J., Chavez-Abril, M.A. (2019). Liquefaction case histories after the 2016 megathrust Pedernales earthquake in Ecuador. In: 7th International Conference on Eartquake Geotechnical Engineering – 7 ICEGE, Rome, Italy, June, 17-20, 2019, pp. 805-820.

Wentz, F.J., van Ballegooy, S., Rollins, K.M., Ashford, S.A., Ol-sen, M.J. (2015). Large Scale Testing of Shallow Ground Improvements using Blast-Induced Liquefaction", In: 6th International Conference on Earthquake Geotechnical Engineering – 6 ICEGE, Christchurch, New Zealand, Nov., 2-4, 2015.

Wissmann, K.J., van Ballegooy, S., Metcalfe, B.C., Dismuke, J.N., Anderson, C.K. (2015). Rammed aggregate pier ground improve-ment as liquefaction method in sandy and silty soils", In: 6th In-ternational Conference on Earthquake Geotechnical Engineering - 6ICEGE, Christchurch, New Zealand, Nov., 2-4.

Ye, L., Kanamori, H., Avouac, J.P., Li, L., Cheung, K.F., Lay, T. (2016). The 16 April 2016, Mw 7.8 (Ms 7.5) Ecuador earthquake: a quasirepeat of the 1942 Ms 7.5 earthquake and partial re-rupture of the 1906 Ms 8.6 Colombia–Ecuador earthquake. Earth Planet. Sci. Lett. 454, pp. 248–258, 2016

Zuffa, G.G., (1985). Optical analyses of arenites: influence of methodology on compositional results. In: Zuffa, G. (Ed.), Provenance of Arenites NATO ASI 148. Dordrecht/Boston/Lancaster, D. Reidel Publishing Company, pp. 165–189.